



# Development of adjoint-based ocean state estimation for the Amundsen and Bellingshausen Seas and ice shelf cavities using MITgcm/ECCO

Yoshihiro Nakayama<sup>1,2</sup>, Dimitris Menemenlis<sup>1</sup>, Ou Wang<sup>1</sup>, Hong Zhang<sup>1</sup>, Ian Fenty<sup>1</sup>, and An T. Nguyen<sup>3</sup>

<sup>1</sup>Jet Propulsion Laboratory, California Institute of Technology, Pasadena, California, USA.

<sup>2</sup>Institute of Low Temperature Science, Hokkaido University, Sapporo, Hokkaido, Japan.

<sup>3</sup>The University of Texas at Austin, Austin, Texas, USA

**Correspondence:** Yoshihiro Nakayama (Yoshihiro.Nakayama@lowtem.hokudai.ac.jp)

**Abstract.** The Antarctic coastal ocean is impacting sea level rise, deep-ocean circulation, marine ecosystems, and global carbon cycle. To better describe and understand these processes and their variability, it is necessary to combine the sparse available observations with best-possible numerical descriptions of ocean circulation. In particular, high ice-shelf melting rates in the Amundsen Sea have attracted many observational campaigns and we now have some limited oceanographic data that capture seasonal and interannual variability during the past decade. One method to combine observations with numerical models that can maximize the information extracted from the sparse observations is the adjoint method, as developed and implemented for global ocean state estimation by the Estimating the Circulation and Climate of the Ocean (ECCO) project. Here, for the first time, we apply the adjoint-model estimation method to a regional configuration of the Amundsen and Bellingshausen Seas, Antarctica, including explicit representation of sub-ice shelf cavities. We utilize observations available during 2010–2014, including ship-based and seal-tagged CTD measurements, moorings, and satellite sea-ice concentration estimates. After 20 iterations of the adjoint-method minimization algorithm, the cost function, here defined as a sum of weighted model-data difference, is reduced by 65% relative to the baseline simulation by adjusting initial conditions, atmospheric forcing, and vertical diffusivity. The sea-ice and ocean components of the cost function are reduced by 59% and 70%, respectively. Major improvements include better representations of (1) Winter Water (WW) characteristics and (2) intrusions of modified Circumpolar Deep Water (mCDW) towards the Pine Island Glacier. Sensitivity experiments show that ~40% and ~10% of improvements in sea ice and ocean state, respectively, can be attributed to the adjustment of air temperature and wind. This study is a preliminary demonstration of adjoint-method optimization with explicit representation of ice-shelf cavity circulation. Despite the 65% cost reduction, substantial model-data discrepancies remain, in particular with annual and interannual variability observed by moorings in front of the Pine Island Ice Shelf. We list a series of possible causes for these residuals, including limitations of the model, the optimization methodology, and observational sampling. In particular, we hypothesize that that residuals could be further reduced if the model could more accurately represent sea ice concentration and coastal polynyas.



## 1 Introduction

The ice shelves and glaciers in the Amundsen Sea (AS) and Bellingshausen Sea (BS) are melting and thinning rapidly with consequences for global sea level rise and changes in ocean circulation and global carbon cycle (e.g., Arrigo et al., 2008; Pritchard et al., 2012; Paolo et al., 2015; Bronselaer et al., 2018; Rignot et al., 2019). Basal melting of these ice shelves is caused by warm modified Circumpolar Deep Water (mCDW, 0.5–1.5°C), which intrudes onto the continental shelf toward ice shelf cavities following submarine glacial troughs (Fig. 1) (e.g., Jacobs et al., 1996; Walker et al., 2007; Jacobs et al., 2011; Nakayama et al., 2013; Walker et al., 2013; Dutrieux et al., 2014). For this reason, multiple oceanographic observational campaigns have been collected by the international community to understand the mechanism of mCDW intrusions onto the AS continental shelf and towards ice shelf cavities. As part of these efforts, we now have some limited oceanographic data that capture seasonal and interannual variability during the past decade (e.g., Jacobs et al., 2011; Nakayama et al., 2013; Dutrieux et al., 2014; Heywood et al., 2016; Kim et al., 2017; Webber et al., 2017; Mallett et al., 2018).

Recent observations as well as modeling studies reveal that mCDW pathways, ice shelf-ocean interaction, the thermocline depth, and ocean bathymetry below Pine Island Ice Shelf (PIIS) are important for controlling the PIIS melt rate (e.g., Schodlok et al., 2012; Dutrieux et al., 2014; De Rydt et al., 2014; St-Laurent et al., 2015; Dinniman et al., 2016; Jourdain et al., 2017; Kimura et al., 2017; Webber et al., 2019). The thermocline depth was ~200 m deeper in 2012 compared to other years (e.g., 1994, 2007, 2009, and 2010, see Fig. 2A in Dutrieux et al. (2014)), which reduced the PIIS melt by ~ 50%. After 2012, the thermocline shoaled by 200m returning to its more commonly observed depth of ~350 m (Webber et al., 2017). It is suggested that this thermocline variability was caused by changes in local and remote surface wind and buoyancy forcing (Dutrieux et al., 2014; Webber et al., 2017).

To better describe and understand these processes and their variability, it is necessary to combine the sparse available observations with best-possible numerical descriptions of ocean circulation. One method to combine observations with numerical models that can maximize the information extracted from the sparse observations is the adjoint method, as developed and implemented for global ocean state estimation by the Estimating the Circulation and Climate of the Ocean (ECCO) project. To date, the ECCO project has produced ocean state estimates based on Circum-Antarctic or global model configurations (e.g., Mazloff et al., 2010; Forget et al., 2015; Zhang et al., 2018; Fukumori et al., 2020). Employing the adjoint model produced by automatic differentiation (Giering and Kaminski, 1998) and utilizing temporally-varying oceanographic observations, these ocean state estimates are capable of simulating the large-scale evolution of the Southern Ocean consistent with the available observations. Many observational and modeling studies have been conducted to understand Southern Ocean gyre dynamics, subsurface ocean circulation, the southern shift of various fronts around Antarctica, etc. (e.g., Gille et al., 2016; Jones et al., 2016; Tamsitt et al., 2017; Nakayama et al., 2018; Roach and Speer, 2019; Jones et al., 2020). However, despite the importance of Antarctic coastal regions for global climate, existing models fail to accurately reproduce the sparse available observations, likely owing to the difficulty in simulating Antarctic continental shelf regions and sub-ice-shelf-cavity processes (Mazloff et al., 2010; Timmermann et al., 2012; Kusahara and Hasumi, 2013; Nakayama et al., 2014; Rodriguez et al., 2016; Nakayama et al., 2017; Kusahara, 2020).



For other regions of the globe, ocean state estimates based on regional configurations have been successfully developed during the past decades, achieving good model-data agreement and leading to understanding of regional processes (Fenty and Heimbach, 2013b,c; Verdy et al., 2014; Rudnick et al., 2015; Nguyen et al., 2020; Verdy et al., 2017; Vinogradova et al., 2014). For Antarctic coastal regions, however, the only previous attempt to constrain a model with observations was the study of Nakayama et al. (2017), which used a low-dimensional estimation approach based on the computation of model Green's functions. Here we aim to extend the study of Nakayama et al. (2017) by employing the adjoint method, which permits a larger number of higher dimension control variables than the Green's Function approach. The objective is to obtain a closer fit to the available observations than what was achieved in Nakayama et al. (2017). This objective is challenging due to several difficulties including (1) polar specific processes (ice shelf and sea ice) are highly nonlinear and (2) observational data is limited. The groundwork for making adjoint-method optimization possible in the presence of ice shelf cavities was laid out in the study of Heimbach and Losch (2012), who obtained adjoint sensitivities of sub-ice shelf melt rates to ocean circulation under Pine Island Ice Shelf, West Antarctica.

In this study, we present our attempt at the development of Amundsen-Bellinghousen Seas ocean state estimates (Fig. 2) by employing the adjoint-model-based data assimilation method developed by ECCO for regional and global ocean state estimation (Mazloff et al., 2010; Forget et al., 2015; Zhang et al., 2018; Fukumori et al., 2020). We focus on the years 2010–2014 when oceanographic observations were collected frequently and the largest interannual variability has been observed (Dutrieux et al., 2014; Webber et al., 2017). Our simulations are carried out for a subregion of the global Latitude-Longitude-Polar-Cap (LLC) 270 configuration (Zhang et al., 2018). As the LLC270 horizontal and vertical resolutions are insufficient to resolve critical ocean-ice shelf interaction processes, e.g., eddy transport, mean flow topography interaction, this study can be regarded as a step toward improved parameterization and adjustment of these processes in future global ECCO optimizations.

## 2 Data and methods

### 2.1 Observations

In the Amundsen Sea, oceanographic observational campaigns were carried out in 2010, 2012, and 2014 (Nakayama et al., 2013; Dutrieux et al., 2014; Heywood et al., 2016; Kim et al., 2017). Several mooring observations were also obtained, with the moorings at the PIIS front capturing the largest interannual variability observed in the region between 2009–2014 (Dutrieux et al., 2014; Webber et al., 2017). We also utilize seal-tagged CTD observations obtained in 2014, which contain over 10,000 profiles between February and November (Heywood et al., 2016). In the central part of the Bellingshausen Sea, no oceanographic observations were collected between 2010–2014. Despite that seal-tagged CTD observations are available (Roquet et al., 2013; Zhang et al., 2016), these datasets are not used in the current version of state optimization. For the Antarctic peninsula region, oceanographic observations were collected by the Palmer Antarctic Long-Term Ecological Research project (PAL-LTER, Ducklow et al. (2012)). For sea ice, we use satellite-based estimates of daily sea ice concentration with grid resolutions of 25 km (Cavalieri et al., 1996). The datasets used in this study are summarized in Figs. 2-3 and Table 1.



## 2.2 Numerical model

We employ the Massachusetts Institute of Technology general circulation model (MITgcm), which includes dynamic/thermodynamic  
90 sea-ice (Losch et al., 2010) and thermodynamic ice shelf (Losch, 2008) capabilities. Following the model configuration from  
Nakayama et al. (2017), we extract the regional grid from a global LLC270 configuration for the AS and BS regions (Fig. 1).  
South of 70°S, the LLC270 configuration uses a bipolar grid; in the AS and BS domain, the horizontal grid spacing is ap-  
proximately 10 km (Fig. 1). The vertical discretization of the ECCO LLC270 configuration comprises 50 levels varying in  
thickness from 10 m near the surface, 70–90 m in the 500–1000-m depth range, and 450 m at the deepest level of 6000 m.  
95 Model bathymetry is derived from the International Bathymetric Chart of the Southern Ocean (IBCSO; Arndt et al. (2013))  
and the model ice draft is based on Antarctic Bedrock Mapping (BEDMAP-2; Fretwell et al. (2013)). Following Nakayama  
et al. (2017), we simulate the effect of the ice barrier (shown in white indicated by the red arrow in Fig. 1) by limiting sea-ice  
transport between the eastern and central AS.

The first guess of the model initial state is a simulated 2010 oceanographic condition based on Green’s function approach  
100 (Nakayama et al., 2017). Lateral boundary conditions for hydrography, currents, and sea ice are provided by the ongoing ECCO  
LLC270 optimization. The initial guess of surface forcing for 2010–2014 period is provided by ERA-Interim (Dee et al., 2011).  
There is no additional freshwater runoff above and beyond the meltwater computed by the MITgcm ice shelf package. The  
model parameters used for this state estimate are shown in Table 2.

The MITgcm 4D-Var assimilation system iteratively minimizes the squared sum of weighted model data misfits and control  
105 adjustments by using the adjoint model to adjust the control variables (Wunsch et al., 2009; Wunsch and Heimbach, 2013). The  
control vector consists of model initial conditions for temperature and salinity, vertical diffusivity, and all atmospheric states  
(air temperature, specific humidity, precipitation, shortwave radiation, longwave radiation, and eastward and northward winds).  
The gradient of the cost function is obtained by integrating the adjoint of the tangent linear model backward in time (Le Dimet  
and Talagrand, 1986) and is used with the quasi-Newton M1QN3 conjugate-gradient algorithm (Gilbert and Lemaréchal, 1989)  
110 to adjust the control variables to iteratively reduce the cost function toward its minimum. Sea ice concentration is constrained  
using a pseudo-sea ice adjoint, whose details are provided in Forget et al. (2015). We also note that background horizontal  
viscosity has to be artificially increased at the early stage of the optimization for model stability and we manually lowered the  
values of viscosity at iterations 10, 15, and 20 (Tables 2 and 3).

For the static ice shelf component, the freezing/melting process in the sub-ice-shelf cavity is parameterized by the three-  
115 equation thermodynamics of Hellmer and Olbers (1989); Jenkins (1991). We use constant turbulent heat and salt exchange  
coefficients for individual ice shelves, which are already adjusted in Nakayama et al. (2017). However, only for Pine Island  
and Thwaites, we further modify these coefficients for simulations after iteration 11 (Table 3), as ice shelf melt rates of Pine  
Island and Thwaites become too large. Changes of these coefficients do not highly alter on-shelf circulation (see Fig. S18 in  
Nakayama et al. (2018)) and adjustments of these coefficients in addition to optimizations based on adjoint sensitivities is  
120 possible.



### 3 Results

#### 3.1 Unoptimized simulation (iteration 0)

As we initialize the unoptimized simulation (iteration 0) with simulated oceanographic conditions based on Green's function approach (Nakayama et al., 2017), its 2010 simulated vertical sections show a good agreement with observations (Fig. 4).  
125 Simulated vertical sections present mCDW below 400–500 m and WW above 250–400 m consistent with observations (Fig. 2 in Jacobs et al. (2011) and Fig. 4 in Nakayama et al. (2013)). Similar to Nakayama et al. (2017), slight differences can still be found for WW properties close to the surface (salinity being still too saline ( $\sim 0.1$  psu)) and PIIS front mCDW properties ( $\sim 0.1$  psu for salinity and  $\sim 0.2^\circ\text{C}$  for potential temperature, Fig. 4).

We find, however, that the time evolution of iteration 0 between 2010–2014 does not agree well with observations. For exam-  
130 ple, oceanographic conditions at the PIIS front in iteration 0 simulation becomes too cold and fresh by  $\sim 2^\circ\text{C}$  and  $\sim 0.25$  psu, respectively (Figs.4 and 5). Furthermore, the horizontal section of potential temperature at 552 m depth illustrates the formation of cold and fresh water masses ( $\sim -1^\circ\text{C}$  and 34.4 psu) in the vicinity of the PIIS (the red arrows in Fig. 6). This water spreads along the coast and induces unrealistic cooling in the large area of the AS (Figs.6 and 7). Simulated time series of potential temperature and salinity at the PIIS front mooring (Fig. 8) shows that these changes occur as a result of intense cooling by the  
135 atmosphere in the austral winter of 2013 and this cooling leads to the reduction of the PIIS melt rate by  $\sim 100$  Gt  $\text{yr}^{-1}$  (Fig. 9a).

#### 3.2 Model–Observation Differences and improvements

As a result of the iterative optimization, we are able to reduce the cost, which is defined as a sum of weighted model-data difference, by 65% by adjusting initial ocean temperature and salinity, atmospheric surface parameters, and vertical diffusivity (Fig. 2). The cost reduction occurs quicker in the first 10 iterations (Fig. 2). Throughout the optimization, sea ice and ocean  
140 costs are reduced by 59% and 70%, respectively.

##### 3.2.1 Sea ice

In the iteration 20 simulation, spatial patterns of the sea ice concentrations show better agreement with observations. For September, simulated sea ice concentration is overestimated in iteration 0 at the northern model boundary but becomes much closer to observations in iteration 20 (Fig. 10). For March, simulated sea ice area is larger by 0.12 million  $\text{km}^2$ , and 0.13 million  
145  $\text{km}^2$  in iteration 0 and 0.08 million  $\text{km}^2$  and 0.05 million  $\text{km}^2$  in iteration 20 in the AS and BS, respectively (Fig. 10).

##### 3.2.2 Ocean

For the AS, there are two major improvements for the oceanographic condition: (1) representation of mCDW intrusions towards the ice shelf cavities and (2) properties of WW. For the BS, we do not include enough observational data in the current version of the ocean state estimate and are not able to judge the capability of our state estimation.



150 As model-data difference becomes larger towards the end of the 2010–2014 simulation for unoptimized simulation, we  
compare 2014 oceanographic conditions between iterations 0 and 20 simulations to assess improvements. At greater depths,  
mCDW penetrates along the submarine glacial troughs towards the Pine Island, Thwaites ice shelf cavities (the red arrows in  
Figs.6a, b) in the iteration 20 simulation, qualitatively similar to observations and other model studies (Jacobs et al., 2011;  
Nakayama et al., 2013; Dutrieux et al., 2014; Nakayama et al., 2018, 2019). The 552-m potential temperature and salinity  
155 difference between iteration 0 and iteration 20 simulations are  $\sim 0.5^\circ\text{C}$  and  $\sim 0.1$  psu along the coast of the AS, respectively  
(Fig. 6). Simulated time series of potential temperature and salinity at the PIIS front mooring also show the continuous intrusion  
of mCDW into the PIIS cavity from 2010–2014, consistent with observations (e.g., Jacobs et al., 2011; Dutrieux et al., 2014;  
Kim et al., 2017; Jenkins et al., 2018; Assmann et al., 2019).

At shallower depths, the thermocline is located deeper by  $\sim 150$  m in the AS in 2014 than in 2010 (Figs.4 and 5), which  
160 seems to be consistent with observations (Jacobs et al., 2011; Nakayama et al., 2013; Dutrieux et al., 2014; Heywood et al.,  
2016). The 222-m salinity difference between iteration 0 and iteration 20 simulations shows freshening by 0.05–0.1 mostly  
everywhere in the AS (the red arrows in Figs. 7d and e). This is a good improvement as WW tends to become too saline in  
most numerical models (e.g., St-Laurent et al., 2015; Nakayama et al., 2018) and good representations of surface hydrographic  
conditions as well as stratification are necessary for the better representation of interannual variabilities.

### 165 3.2.3 Ice shelf

Heat and salt transfer coefficients are kept constant and we do not allow them to change over time. Thus, time series of ice shelf  
melt rates simply reflect changes of oceanographic conditions in the ice shelf cavities. We note, however, that these coefficients  
are adjusted once at iteration 11 for Pine Island and Thwaites ice shelves (Tables 3 and 4). In iteration 0, simulated time series  
of Pine Island and Thwaites ice shelf melt rates show a reduction of  $\sim 100$  Gt  $\text{yr}^{-1}$  between 2010–2014 (Fig. 9). In the iteration  
170 20 simulation, however, both time series of Pine Island and Thwaites ice shelf melt rates become rather stable at  $\sim 110$  Gt  
 $\text{yr}^{-1}$  but show slight decreasing trends of  $\sim 4$  Gt  $\text{yr}^{-2}$  and  $\sim 3$  Gt  $\text{yr}^{-2}$ , respectively. Simulated Pine Island melt rate shows a  
reduction in 2012 by  $\sim 30$  Gt  $\text{yr}^{-1}$  and simulated Thwaites melt rate shows reductions of  $\sim 20$  Gt  $\text{yr}^{-1}$  and  $\sim 50$  Gt  $\text{yr}^{-1}$  in  
2012 and 2013, respectively. For ice shelves in the BS, melt rates remain almost constant (e.g., Fig .9).

Based on observations, it is suggested that melt rates of Pine Island and Thwaites ice shelves should have decreased between  
175 2012–2014 due to deepened thermocline (Dutrieux et al., 2014; Webber et al., 2017) and estimated ice shelf melt rates from  
oceanographic observations are  $\sim 75$  Gt  $\text{yr}^{-1}$  and  $\sim 40$  Gt  $\text{yr}^{-1}$  based on 2009/2010 and 2012/2014 observations, respectively.  
However, these estimates rely on single snapshots of ice shelf front oceanographic observations. Satellite-based estimates of  
ice shelf melt rates are 101 Gt  $\text{yr}^{-1}$  and 98 Gt  $\text{yr}^{-1}$  for Pine Island and Thwaites ice shelves, respectively. These estimates are  
derived from volume flux divergence of Antarctic ice shelves in 2007 and 2008 with 1979 to 2010 surface accumulation and  
180 2003 to 2008 thinning (Rignot et al., 2013) and may represent ice shelf melt rates in warm oceanographic conditions in the  
eastern AS.

In general, heat and salt transfer coefficients are already adjusted in Nakayama et al. (2017), and melt rates of ice shelves  
in the AS and BS are consistent with satellite-based estimates (Table 4). The interannual variability of the simulated ice shelf



185 melt rates may be too weakened compared to observations possibly because (1) coarse horizontal and vertical grids used in  
this configuration may not allow the realistic representation of ocean cavity circulation and/or (2) observed reduction of ice  
shelf melt rates are caused by changes in ice shelf geometry and it can not be simulated in static ice shelf cavity configuration.  
Satellite based estimates of time-evolving ice shelf melt rates are required for further comparison.

## 4 Discussion

### 4.1 Sensitivity studies

190 To investigate the reason for the improvements, we conducted 3 sensitivity experiments (Table 5) as air temperature, precip-  
itation, and wind are considered to be main drivers of oceanographic variabilities at the PIIS front region. The total costs are  
 $2.9 \times 10^6$ ,  $3.1 \times 10^6$ ,  $2.9 \times 10^6$ , and  $4.1 \times 10^6$  for iteration 20, NoWindAdj, NoPrepAdj, and NoAtempAdj cases, respectively  
showing that adjustments of wind and atmospheric temperature play important roles for reducing both sea ice and ocean  
costs. Sea ice costs are  $1.7 \times 10^6$ ,  $1.6 \times 10^6$ ,  $1.7 \times 10^6$ , and  $2.9 \times 10^6$  for iteration 20, NoWindAdj, NoPrepAdj, and NoAtempAdj  
195 cases, respectively. Ocean costs are  $1.1 \times 10^6$ ,  $1.5 \times 10^6$ ,  $1.1 \times 10^6$ , and  $1.2 \times 10^6$  for iteration 20, NoWindAdj, NoPrepAdj, and  
NoAtempAdj cases, respectively. This implies that adjustment of wind has the strongest impact on the ocean, while adjustment  
of air temperature has the strongest impact on sea ice.

Among these sensitivity experiments, the 2014 January mean potential temperature at 552 m depth shows a similar spatial  
pattern for all cases for open ocean and in the BS (not shown) and differences can only be found in the AS especially at the  
200 PIIS front (Fig. 11). Spatially averaged 552 m potential temperatures at the PIIS front (averaged for the region enclosed by red  
box in Fig 11a) are  $0.61^\circ\text{C}$ ,  $0.23^\circ\text{C}$ ,  $0.56^\circ\text{C}$ , and  $0.53^\circ\text{C}$  for iteration 20 NoWindAdj, NoPrepAdj, and NoAtempAdj cases,  
respectively. Vertically integrated heat contents, which are strongly controlled by thermocline depth (Nakayama et al., 2018),  
reduced by 11%, 5%, and 12%, respectively, for NoWindAdj, NoPrepAdj, and NoAtempAdj cases compared to iteration 20  
solution. This implies that (1) PIIS front mCDW temperature and thus mCDW pathways as well as strength of intrusions are  
205 dominantly controlled by wind and (2) the PIIS front thermocline depth is influenced rather equally by wind, precipitation, and  
air temperature.

### 4.2 Seasonal and interannual variability

Mooring observations at the PIIS front were conducted from 2009–2014, which provide us potential temperature measurements  
at various depths (Webber et al., 2017). At depths below 800 m, the observed potential temperature remains rather stable at  
210  $\sim 1^\circ\text{C}$  (Fig. 12c). At 600–700 m depths, the potential temperature also remains stable at  $1^\circ\text{C}$  and shows gradual cooling and  
warming between 2010–2012 and 2013–2015, respectively (Fig. 12). Between 2012–2013, however, potential temperature time  
series shows sporadic emergence of cold watermass ( $\sim -0.5^\circ\text{C}$ ). At 400–500 m depths, the time series of potential temperature  
fluctuates between  $-1.8^\circ\text{C}$  and  $0^\circ\text{C}$  and seasonal and interannual variabilities are large.



For iteration 0, we find three major differences with respect to the observations (Fig. 12); (1) simulated potential temperature shows rapid cooling between 2013–2015 and potential temperature at all depths changes from  $\sim 1^\circ\text{C}$  to  $\sim -1^\circ\text{C}$ , (2) simulated time series of potential temperature shows sudden emergence of cold water at all depths throughout the simulated period, while it occurs only for shallower depths for observations, and (3) timing of cooling and warming do not agree with observations. This sporadic coolings are likely associated with strong wind events which lead to the formation of cold and dense water and deep convection.

For the iteration-20 simulation, simulated timeseries show improvements at all depths (Fig. 12). At greater depths (800–900 m), the potential temperature remains rather stable at  $\sim 1^\circ\text{C}$  consistent observations (Fig. 12c) and the sudden emergence of cold water only occurs at shallower depths. However, the long term and short term variabilities have large differences between observations and the iteration-20 simulation, and the timing of cooling and warming still do not agree with observations. One possible reason for the difference is deficiencies in the simulated sea ice concentration near the coast. In our current configuration using a pseudo-sea-ice adjoint sensitivity, we are not able to directly adjust sea ice concentration: simulated sea ice concentration at the PIIS front remains almost the same between the iteration 0 and iteration-20 simulations (Fig. 12).

## 5 Conclusions

In the previous work, Nakayama et al. (2017) employed a Green's function approach to adjust a numerical simulation of 2010 AS conditions close to observations. However, we find that continuation of the Nakayama et al. (2017) set-up until the year 2014 leads to unrealistic cooling and freshening at the PIIS front and other coastal regions of the AS (Figs. 4–6, 8).

In this work, we develop an Amundsen Bellingshausen Sea ocean simulation following Nakayama et al. (2017) and employ the ECCO ocean state estimation tools based on adjoint sensitivities (Forget et al., 2015; Zhang et al., 2018) to develop an ocean state estimate for the AS and BS for the time period of 2010–2014. We choose this time window because the largest interannual variability was observed after first observations in 1994 (Dutrieux et al., 2014) and a good amount of oceanographic observations is available. After 20 iterations, cost, which is defined as a sum of weighted model-data difference, is reduced by 65% by adjusting initial condition, atmospheric forcing, and vertical diffusivity (Fig. 2). The iteration 20 simulation can simulate oceanographic conditions much closer to observations for the 2010–2014 period compared to the unoptimized iteration 0 simulation. The main improvements are (1) simulated sea ice extent for the AS and BS, (2) simulated WW properties and thermocline depths in the AS, and (3) simulated mCDW intrusions towards AS ice shelf cavities and their pathways (Figs. 5–7). Despite the improvements listed above, seasonal and interannual variability of oceanographic conditions at the PIIS front is not simulated well compared to the mooring observations and it remains difficult to simulate seasonal and interannual changes of oceanographic conditions on the AS continental shelf (Fig. 12).

There are several lines of investigation that can improve upon the technical foundation discussed hereinabove. This includes new sea-ice adjoint optimization code (Fenty and Heimbach, 2013a; Bigdeli et al., 2020), improved methods of calculating costs to put more emphasis on the seasonal and interannual variabilities (Forget et al., 2015), adding other oceanographic datasets not used in the current optimization such as moorings and instrumented pinnipeds (Roquet et al., 2013; Assmann





et al., 2019), and more careful estimation of model and data prior uncertainty. Considering the grid resolution selected for this regional model (10-km horizontal grid spacing), this work is a step towards the improved representation of ice-shelf ocean interaction in the ECCO (Estimating the Circulation and Climate of the Ocean) global ocean retrospective analysis as well as  
250 current-generation IPCC (Intergovernmental Panel on Climate Change) global climate models.

*Data availability.* The model code, input, and results of iteration 20 are available at <https://doi.org/10.5281/zenodo.4541036>. They are also available at [https://ecco.jpl.nasa.gov/drive/files/ECCO2/LLC270/ABS\\_ADJOINT/results](https://ecco.jpl.nasa.gov/drive/files/ECCO2/LLC270/ABS_ADJOINT/results).

*Author contributions.* Y.N. conceived the study, conducted the ocean modeling, and wrote the initial draft of the paper. D.M., O.W., H.Z., and A.N. contributed to the technical development of regional Amundsen and Bellingshausen optimization. Y.N., D.M., O.W., H.Z., A.N.,  
255 and I.F. discussed the results and implications and commented on the manuscript at all stages.

*Competing interests.* The authors declare no competing interests.

*Acknowledgements.* The research was carried out at the Jet Propulsion Laboratory, California Institute of Technology, under a contract with the National Aeronautics and Space Administration (NASA). Support was provided by an appointment to the NASA Postdoctoral Program; the NASA Cryosphere program; and the NASA Modeling, Analysis, and Prediction program. Computations were carried out at the NASA  
260 Advanced Supercomputing facilities. This work was also supported by the fund from Grant in Aids for Scientific Research (19K23447) of the Japanese Ministry of Education, Culture, Sports, Science, and Technology. We thank Karen Heywood, Ben Webber, Stan Jacobs, Tae Wan Kim, Catherine Walker for their support for finding and accessing observational datasets. We also thank Patrick Heimbach, Martin Losch, and Matthew Mazloff for their technical suggestions.



## References

- 265 Arndt, J. E., Schenke, H. W., Jakobsson, M., Nitsche, F. O., Buys, G., Goleby, B., Rebesco, M., Bohoyo, F., Hong, J., Black, J., et al.: The International Bathymetric Chart of the Southern Ocean (IBCSO) Version 1.0 A new bathymetric compilation covering circum-Antarctic waters, *Geophysical Research Letters*, 40, 3111–3117, 2013.
- Arrigo, K. R., van Dijken, G., and Long, M.: Coastal Southern Ocean: A strong anthropogenic CO<sub>2</sub> sink, *Geophysical Research Letters*, 35, 2008.
- 270 Assmann, K., Darelius, E., Wåhlin, A. K., Kim, T.-W., and Lee, S. H.: Warm Circumpolar Deep Water at the Western Getz Ice Shelf Front, Antarctica, *Geophysical Research Letters*, 46, 870–878, 2019.
- Bigdeli, A., Nguyen, A. T., Pillar, H., Ocaña, V., and Heimbach, P.: Atmospheric Warming Drives Growth in Arctic Sea-Ice: A Key Role for Snow, *Geophys. Res. Lett.*, 47, <https://doi.org/10.1029/2020GL090236>, 2020.
- Bronselaer, B., Winton, M., Griffies, S. M., Hurlin, W. J., Rodgers, K. B., Sergienko, O. V., Stouffer, R. J., and Russell, J. L.: Change in  
275 future climate due to Antarctic meltwater, *Nature*, 564, 53–58, 2018.
- Cavalieri, D., Parkinson, C., Gloersen, P., and Zwally, H.: Sea ice concentrations from Nimbus-7 SMMR and DMSP SSM/I passive microwave data, January 1979–June 2006, Boulder, Colorado USA: National Snow and Ice Data Center, digital media, 1996.
- De Rydt, J., Holland, P., Dutrieux, P., and Jenkins, A.: Geometric and oceanographic controls on melting beneath Pine Island Glacier, *Journal of Geophysical Research: Oceans*, 119, 2420–2438, 2014.
- 280 Dee, D., Uppala, S., Simmons, A., Berrisford, P., Poli, P., Kobayashi, S., Andrae, U., Balmaseda, M., Balsamo, G., Bauer, P., et al.: The ERA-Interim reanalysis: Configuration and performance of the data assimilation system, *Quarterly Journal of the Royal Meteorological Society*, 137, 553–597, 2011.
- Dinniman, M. S., Asay-Davis, X. S., Galton-Fenzi, B. K., Holland, P. R., Jenkins, A., and Timmermann, R.: Modeling ice shelf/ocean interaction in Antarctica: A review, *Oceanography*, 29, 144–153, 2016.
- 285 Ducklow, H., Clarke, A., Dickhut, R., Doney, S. C., Geisz, H., Huang, K., Martinson, D. G., Meredith, M. P., Moeller, H. V., Montes-Hugo, M., et al.: The marine system of the Western Antarctic Peninsula, *Antarctic ecosystems: an extreme environment in a changing world*, pp. 121–159, 2012.
- Dutrieux, P., De Rydt, J., Jenkins, A., Holland, P. R., Ha, H. K., Lee, S. H., Steig, E. J., Ding, Q., Abrahamsen, E. P., and Schröder, M.: Strong sensitivity of Pine Island ice-shelf melting to climatic variability, *Science*, 343, 174–178, 2014.
- 290 Fenty, I. and Heimbach, P.: Coupled sea ice–ocean–state estimation in the Labrador Sea and Baffin Bay, *Journal of physical oceanography*, 43, 884–904, 2013a.
- Fenty, I. and Heimbach, P.: Hydrographic preconditioning for seasonal sea ice anomalies in the Labrador Sea, *Journal of physical oceanography*, 43, 863–883, 2013b.
- Fenty, I. and Heimbach, P.: Coupled sea ice–ocean–state estimation in the Labrador Sea and Baffin Bay, *Journal of physical oceanography*,  
295 43, 884–904, 2013c.
- Forget, G., Campin, J.-M., Heimbach, P., Hill, C., Ponte, R., and Wunsch, C.: ECCO version 4: an integrated framework for non-linear inverse modeling and global ocean state estimation, 2015.
- Fretwell, P., Pritchard, H. D., Vaughan, D. G., Bamber, J., Barrand, N., Bell, R., Bianchi, C., Bingham, R., Blankenship, D., Casassa, G., et al.: Bedmap2: improved ice bed, surface and thickness datasets for Antarctica, *The Cryosphere*, 7, 2013.



- 300 Fukumori, I., Wang, O., Fenty, I., Forget, G., Heimbach, P., and Ponte, R. M.: Synopsis of the ECCO Central Production Global Ocean and  
Sea-Ice State Estimate, <https://doi.org/10.5281/zenodo.3765929>, <https://doi.org/10.5281/zenodo.3765929>, 2020.
- Giering, R. and Kaminski, T.: Recipes for adjoint code construction, *ACM Transactions on Mathematical Software (TOMS)*, 24, 437–474,  
1998.
- Gilbert, J. C. and Lemaréchal, C.: Some numerical experiments with variable-storage quasi-Newton algorithms, *Mathematical programming*,  
305 45, 407–435, 1989.
- Gille, S. T., McKee, D. C., and Martinson, D. G.: Temporal Changes in the Antarctic Circumpolar Current, *Oceanography*, 29, 96, 2016.
- Heimbach, P. and Losch, M.: Adjoint sensitivities of sub-ice shelf melt rates to ocean circulation under Pine Island Ice Shelf, West Antarctica,  
*Annals of Glaciology*, 53, 59–69, 2012.
- Hellmer, H. and Olbers, D.: A two-dimensional model for the thermohaline circulation under an ice shelf, *Antarctic Science*, 1, 325–336,  
310 1989.
- Heywood, K. J., Biddle, L. C., Boehme, L., Dutrieux, P., Fedak, M., Jenkins, A., Jones, R. W., Kaiser, J., Mallett, H., Garabato, A. C. N.,  
et al.: Between the devil and the deep blue sea: the role of the Amundsen Sea continental shelf in exchanges between ocean and ice  
shelves, *Oceanography*, 29, 118–129, 2016.
- Jacobs, S. S., Hellmer, H. H., and Jenkins, A.: Antarctic ice sheet melting in the Southeast Pacific, *Geophysical Research Letters*, 23, 957–  
315 960, 1996.
- Jacobs, S. S., Jenkins, A., Giulivi, C. F., and Dutrieux, P.: Stronger ocean circulation and increased melting under Pine Island Glacier ice  
shelf, *Nat. Geosci.*, 4, 519–523, 2011.
- Jenkins, A.: A one-dimensional model of ice shelf-ocean interaction, *Journal of Geophysical Research: Oceans*, 96, 20 671–20 677, 1991.
- Jenkins, A., Shoosmith, D., Dutrieux, P., Jacobs, S., Kim, T. W., Lee, S. H., Ha, H. K., and Stammerjohn, S.: West Antarctic Ice Sheet retreat  
320 in the Amundsen Sea driven by decadal oceanic variability, *Nature Geoscience*, 11, 733–738, 2018.
- Jones, D. C., Meijers, A. J., Shuckburgh, E., Sallée, J.-B., Haynes, P., McAufield, E. K., and Mazloff, M. R.: How does Subantarctic Mode  
Water ventilate the Southern Hemisphere subtropics?, *Journal of Geophysical Research: Oceans*, 121, 6558–6582, 2016.
- Jones, D. C., Boland, E., Meijers, A. J., Forget, G., Josey, S., Sallée, J.-B., and Shuckburgh, E.: The sensitivity of Southeast Pacific heat  
distribution to local and remote changes in ocean properties, *Journal of Physical Oceanography*, 50, 773–790, 2020.
- 325 Jourdain, N. C., Mathiot, P., Merino, N., Durand, G., Le Sommer, J., Spence, P., Dutrieux, P., and Madec, G.: Ocean circulation and sea-ice  
thinning induced by melting ice shelves in the Amundsen Sea, *Journal of Geophysical Research: Oceans*, 122, 2550–2573, 2017.
- Kim, T.-W., Ha, H. K., Wählin, A., Lee, S., Kim, C.-S., Lee, J. H., and Cho, Y.-K.: Is Ekman pumping responsible for the seasonal variation  
of warm circumpolar deep water in the Amundsen Sea?, *Continental Shelf Research*, 132, 38–48, 2017.
- Kimura, S., Jenkins, A., Regan, H., Holland, P. R., Assmann, K. M., Whitt, D. B., Van Wessem, M., van de Berg, W. J., Reijmer, C. H., and  
330 Dutrieux, P.: Oceanographic controls on the variability of ice-shelf basal melting and circulation of glacial meltwater in the Amundsen  
Sea Embayment, Antarctica, *Journal of Geophysical Research: Oceans*, 122, 10 131–10 155, 2017.
- Kusahara, K.: Interannual-to-Multidecadal Responses of Antarctic Ice Shelf–Ocean Interaction and Coastal Water Masses during the Twen-  
tieth Century and the Early Twenty-First Century to Dynamic and Thermodynamic Forcing, *Journal of Climate*, 33, 4941–4973, 2020.
- Kusahara, K. and Hasumi, H.: Modeling Antarctic ice shelf responses to future climate changes and impacts on the ocean, *Journal of*  
335 *Geophysical Research: Oceans*, 118, 2454–2475, 2013.
- Le Dimet, F.-X. and Talagrand, O.: Variational algorithms for analysis and assimilation of meteorological observations: theoretical aspects,  
*Tellus A: Dynamic Meteorology and Oceanography*, 38, 97–110, 1986.



- Losch, M.: Modeling ice shelf cavities in a z coordinate ocean general circulation model, *Journal of Geophysical Research: Oceans*, 113, 2008.
- 340 Losch, M., Menemenlis, D., Heimbach, P., Campin, J.-M., and Hill, C.: On the formulation of sea-ice models. Part 1: Effects of different solver implementations and parameterizations, *Ocean Model.*, 33, 129–144, 2010.
- Mallett, H. K., Boehme, L., Fedak, M., Heywood, K. J., Stevens, D. P., and Roquet, F.: Variation in the distribution and properties of Circumpolar Deep Water in the eastern Amundsen Sea, on seasonal timescales, using seal-borne tags, *Geophysical Research Letters*, 45, 4982–4990, 2018.
- 345 Mazloff, M. R., Heimbach, P., and Wunsch, C.: An eddy-permitting Southern Ocean state estimate, *Journal of Physical Oceanography*, 40, 880–899, 2010.
- Nakayama, Y., Schröder, M., and Hellmer, H. H.: From circumpolar deep water to the glacial meltwater plume on the eastern Amundsen Shelf, *Deep Sea Res. I*, 77, 50–62, 2013.
- Nakayama, Y., Timmermann, R., Schröder, M., and Hellmer, H.: On the difficulty of modeling Circumpolar Deep Water intrusions onto the  
350 Amundsen Sea continental shelf, *Ocean Modelling*, 84, 26–34, 2014.
- Nakayama, Y., Menemenlis, D., Schodlok, M., and Rignot, E.: Amundsen and Bellingshausen Seas simulation with optimized ocean, sea ice, and thermodynamic ice shelf model parameters, *Journal of Geophysical Research: Oceans*, 122, 6180–6195, 2017.
- Nakayama, Y., Menemenlis, D., Zhang, H., Schodlok, M., and Rignot, E.: Origin of Circumpolar Deep Water intruding onto the Amundsen and Bellingshausen Sea continental shelves, *Nature communications*, 9, 1–9, 2018.
- 355 Nakayama, Y., Manucharayan, G., Kelin, P., Torres, H. G., Schodlok, M., Rignot, E., Dutrieux, P., and Menemenlis, D.: Pathway of Circumpolar Deep Water into Pine Island and Thwaites ice shelf cavities and to their grounding lines, *Scientific Reports*, 2019.
- Nguyen, A. T., Pillar, H., Ocana, V., Bigdeli, A., Smith, T. A., and Heimbach, P.: The Arctic Subpolar gyre sTate Estimate (ASTE): Description and assessment of a data-constrained, dynamically consistent ocean-sea ice estimate for 2002–2017, *J. Adv. Model. Earth Syst.*, <https://doi.org/10.1002/essoar.10504669.3>, submitted, 2020.
- 360 Paolo, F. S., Fricker, H. A., and Padman, L.: Volume loss from Antarctic ice shelves is accelerating, *Science*, 348, 327–331, 2015.
- Pritchard, H. D., Ligtenberg, S. R. M., Fricker, H. A., Vaughan, D. G., Van den Broeke, M. R., and Padman, L.: Antarctic ice-sheet loss driven by basal melting of ice shelves, *Nature*, 484, 502–505, 2012.
- Rignot, E., Jacobs, S. S., Mouginot, J., and Scheuchl, B.: Ice-shelf melting around Antarctica, *Science Express*, 341, 226–270, 2013.
- Rignot, E., Mouginot, J., Scheuchl, B., van den Broeke, M., van Wessel, M. J., and Morlighem, M.: Four decades of Antarctic Ice Sheet  
365 mass balance from 1979–2017, *Proceedings of the National Academy of Sciences*, 116, 1095–1103, 2019.
- Roach, C. J. and Speer, K.: Exchange of water between the Ross Gyre and ACC assessed by Lagrangian particle tracking, *Journal of Geophysical Research: Oceans*, 124, 4631–4643, 2019.
- Rodriguez, A. R., Mazloff, M. R., and Gille, S. T.: An oceanic heat transport pathway to the Amundsen Sea Embayment, *Journal of Geophysical Research: Oceans*, 2016.
- 370 Roquet, F., Wunsch, C., Forget, G., Heimbach, P., Guinet, C., Reverdin, G., Charrassin, J.-B., Bailleul, F., Costa, D. P., Huckstadt, L. A., et al.: Estimates of the Southern Ocean general circulation improved by animal-borne instruments, *Geophysical Research Letters*, 40, 6176–6180, 2013.
- Rudnick, D. L., Gopalakrishnan, G., and Cornuelle, B. D.: Cyclonic eddies in the Gulf of Mexico: Observations by underwater gliders and simulations by numerical model, *Journal of Physical Oceanography*, 45, 313–326, 2015.



- 375 Schodlok, M. P., Menemenlis, D., Rignot, E., and Studinger, M.: Sensitivity of the ice shelf ocean system to the sub-ice shelf cavity shape measured by NASA IceBridge in Pine Island Glacier, West Antarctica, *Annals of Glaciology*, 53, 156–162, 2012.
- St-Laurent, P., Klinck, J., and Dinniman, M.: Impact of local winter cooling on the melt of Pine Island Glacier, Antarctica, *Journal of Geophysical Research: Oceans*, 120, 6718–6732, 2015.
- Tamsitt, V., Drake, H. F., Morrison, A. K., Talley, L. D., Dufour, C. O., Gray, A. R., Griffies, S. M., Mazloff, M. R., Sarmiento, J. L., Wang, J., et al.: Spiraling pathways of global deep waters to the surface of the Southern Ocean, *Nature communications*, 8, 1–10, 2017.
- 380 Timmermann, R., Wang, Q., and Hellmer, H.: Ice-shelf basal melting in a global finite-element sea-ice/ice-shelf/ocean model, *Annals of Glaciology*, 53, 303–314, 2012.
- Verdy, A., Mazloff, M. R., Cornuelle, B. D., and Kim, S. Y.: Wind-driven sea level variability on the California coast: An adjoint sensitivity analysis, *Journal of physical oceanography*, 44, 297–318, 2014.
- 385 Verdy, A., Cornuelle, B., Mazloff, M. R., and Rudnick, D. L.: Estimation of the tropical Pacific Ocean state 2010–13, *Journal of Atmospheric and Oceanic Technology*, 34, 1501–1517, 2017.
- Vinogradova, N. T., Ponte, R. M., Fukumori, I., and Wang, O.: Estimating satellite salinity errors for assimilation of Aquarius and SMOS data into climate models, *Journal of Geophysical Research: Oceans*, 119, 4732–4744, 2014.
- Walker, D. P., Brandon, M. A., Jenkins, A., Allen, J. T., Dowdeswell, J. A., and Evans, J.: Oceanic heat transport onto the Amundsen Sea shelf through a submarine glacial trough, *Geophysical research letters*, 34, 1–4, 2007.
- 390 Walker, D. P., Jenkins, A., Assmann, K. M., Shoosmith, D. R., and Brandon, M. A.: Oceanographic observations at the shelf break of the Amundsen Sea, Antarctica, *J. Geophys. Res.*, 118, 2906–2918, 2013.
- Webber, B. G., Heywood, K. J., Stevens, D. P., Dutrieux, P., Abrahamsen, E. P., Jenkins, A., Jacobs, S. S., Ha, H. K., Lee, S. H., and Kim, T. W.: Mechanisms driving variability in the ocean forcing of Pine Island Glacier, *Nature communications*, 8, 1–8, 2017.
- 395 Webber, B. G., Heywood, K. J., Stevens, D. P., and Assmann, K. M.: The impact of overturning and horizontal circulation in Pine Island Trough on ice shelf melt in the eastern Amundsen Sea, *Journal of Physical Oceanography*, 49, 63–83, 2019.
- Wunsch, C. and Heimbach, P.: Dynamically and kinematically consistent global ocean circulation and ice state estimates, in: *International Geophysics*, vol. 103, pp. 553–579, Elsevier, 2013.
- Wunsch, C., Heimbach, P., Ponte, R. M., Fukumori, I., and MEMBERS, E.-G. C.: The global general circulation of the ocean estimated by the ECCO-Consortium, *Oceanography*, 22, 88–103, 2009.
- 400 Zhang, H., Menemenlis, D., and Fenty, I.: ECCO LLC270 Ocean-Ice State Estimate, 2018.
- Zhang, X., Thompson, A. F., Flexas, M. M., Roquet, F., and Bornemann, H.: Circulation and meltwater distribution in the Bellingshausen Sea: from shelf break to coast, *Geophysical Research Letters*, 2016.

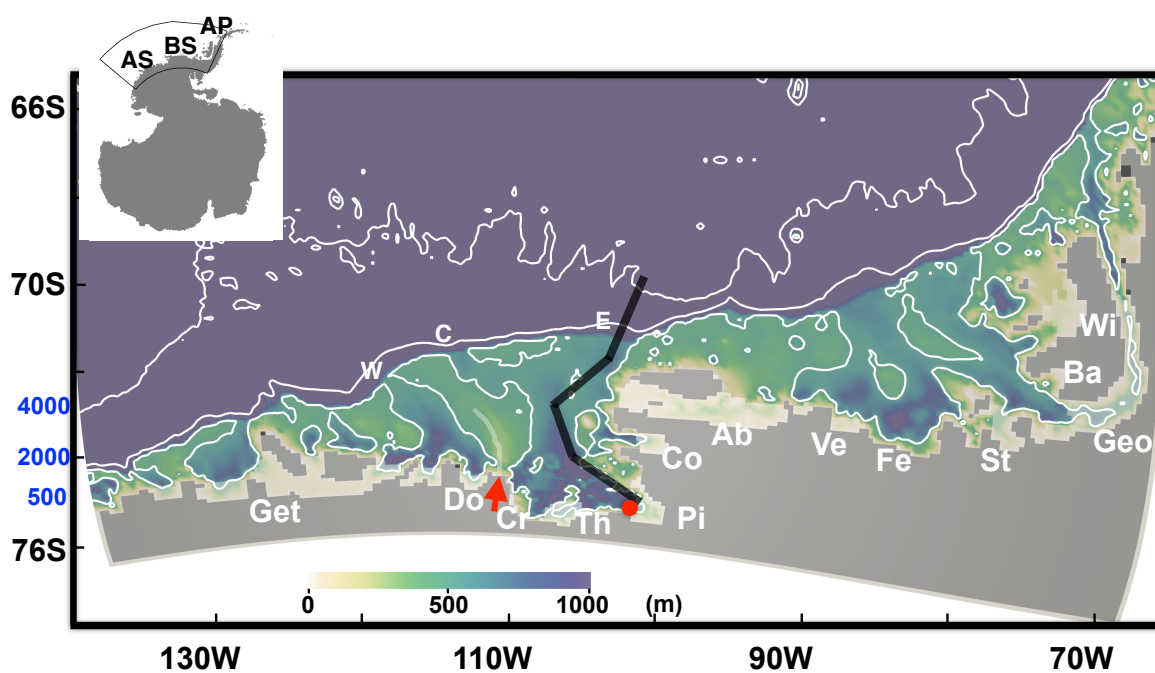


**Figure 1.** Model bathymetry (color) with contours of 500, 2000, and 4000 m in white. The inset (left top) shows Antarctica with the region surrounded by a black line denoting the location of the enlarged portion. AS, BS, and AP denote the Amundsen Sea, Bellingshausen Sea, and Antarctic Peninsula region, respectively. The ice shelves are indicated with transparent white patches and acronyms are summarized in Table 4. Letters E, C, and W denote the submarine glacial troughs located on the eastern AS continental shelf. Transparent white patches (see the red arrow between Do and Cr) indicates the location of grounded icebergs and landfast ice. This white region is treated as a barrier in the sea ice model and we do not allow sea ice exchange crossing this region. The thick black line represents the vertical section shown in Figs. 4 and 5.

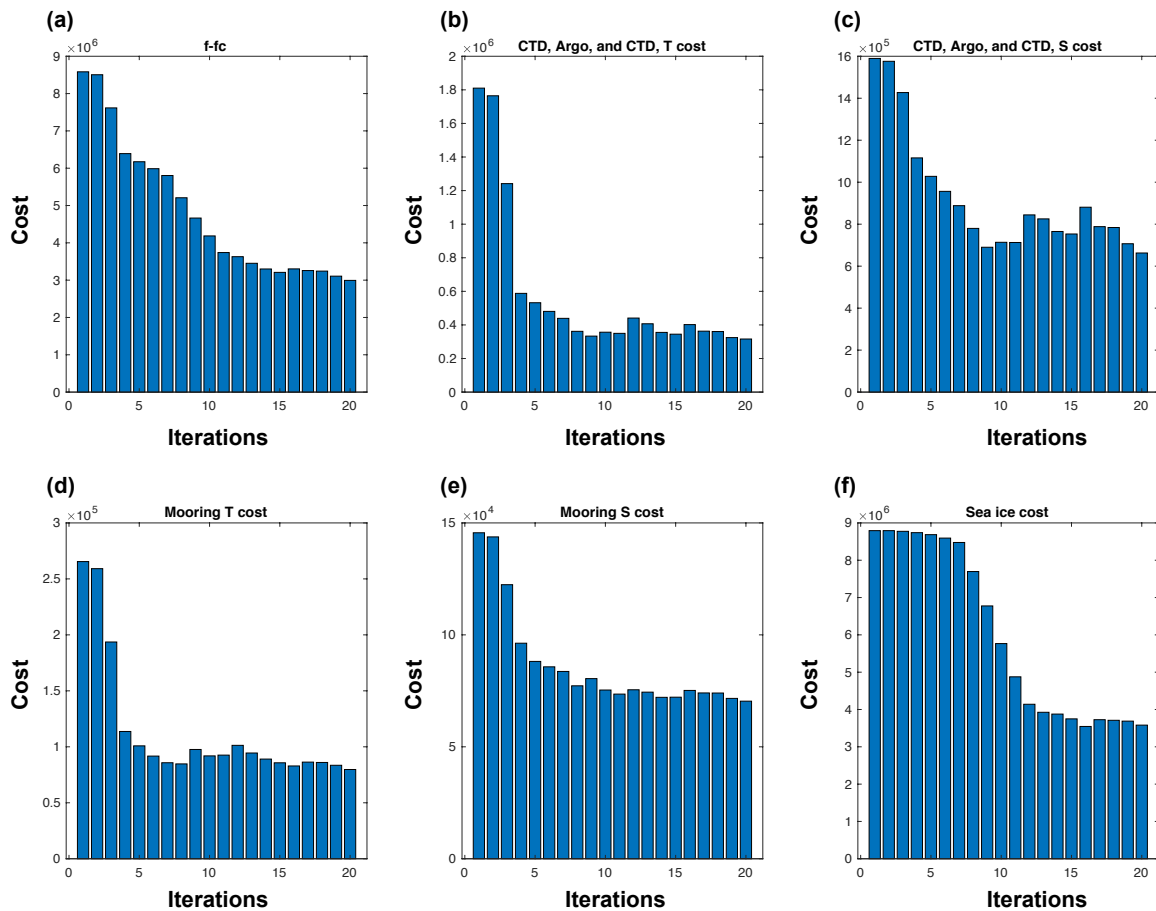


**Figure 2.** Evolution of (a) total, (b) ship-based, Argo, and seal-tagged CTD temperature, (c) ship-based, Argo, and seal-tagged CTD salinity, (d) mooring temperature, (e) mooring salinity, and (f) sea ice costs.

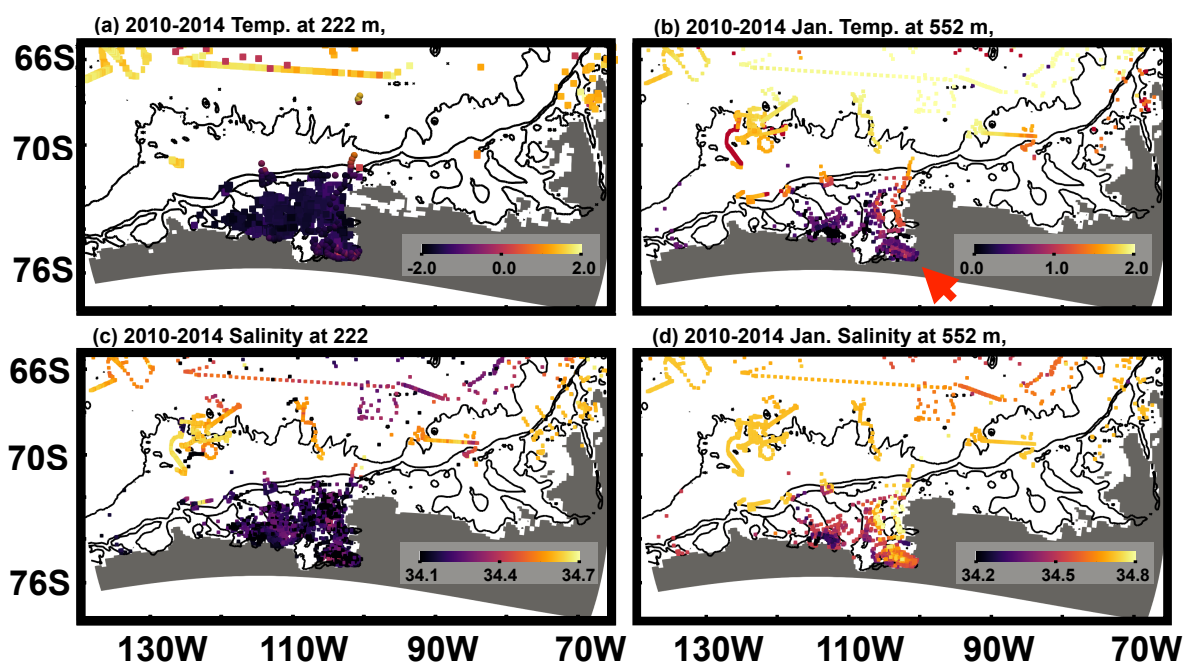


**Figure 3.** (a) 222-m and (b) 552-m potential temperature used for model-data difference calculation and (c) 222-m and (d) 552-m salinity used for model-data difference calculations. Bathymetric contours of 500, 2000, and 4000 m are shown in black. The red arrow indicates the PIIS front region.



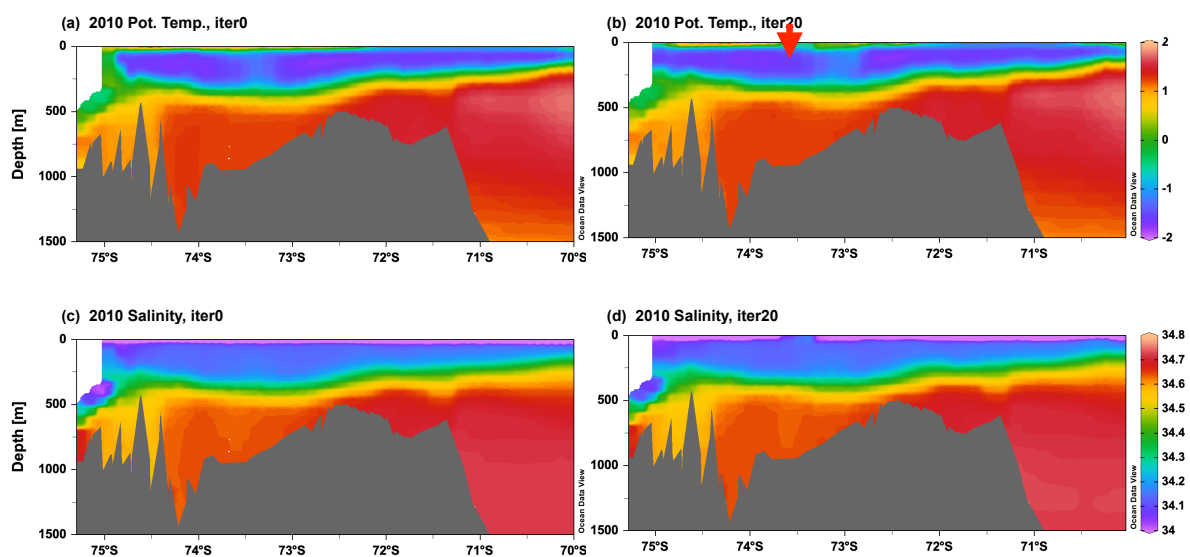


**Figure 4.** Simulated vertical sections of monthly mean potential temperature (top) and salinity (bottom) in January 2010 along the thick black line in Figure 1 for the (left) unoptimized and (right) iteration 20 simulations. The red arrow indicates the central part of the AS where thermocline depth is compared.

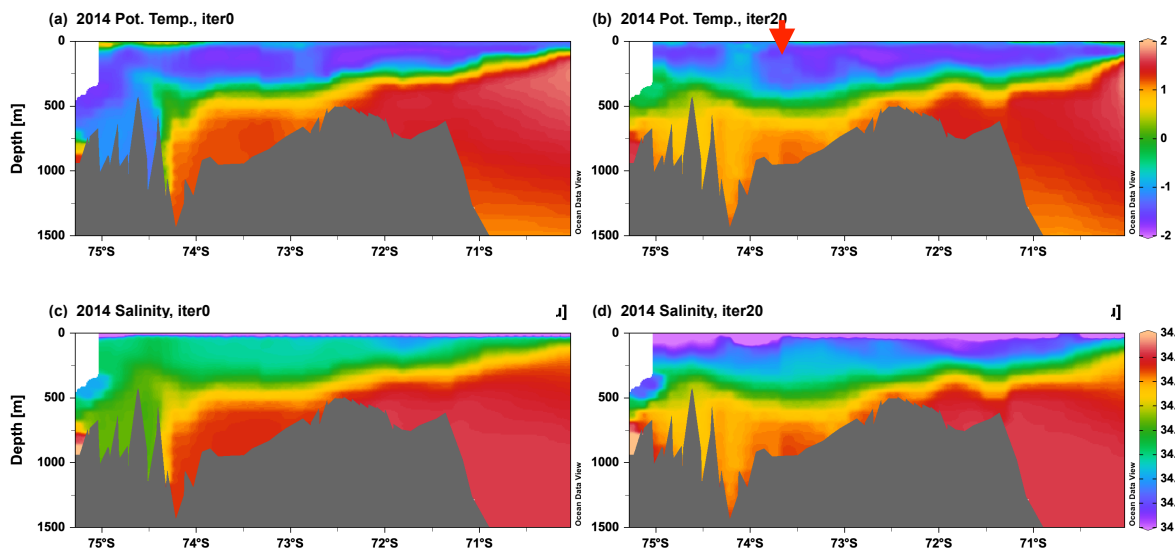


**Figure 5.** Simulated vertical sections of monthly mean potential temperature (top) and salinity (bottom) in January 2014 along the thick black line in Figure 1 for the (left) unoptimized and (right) iteration 20 simulations. The red arrow indicates the central part of the AS where thermocline depth is compared.

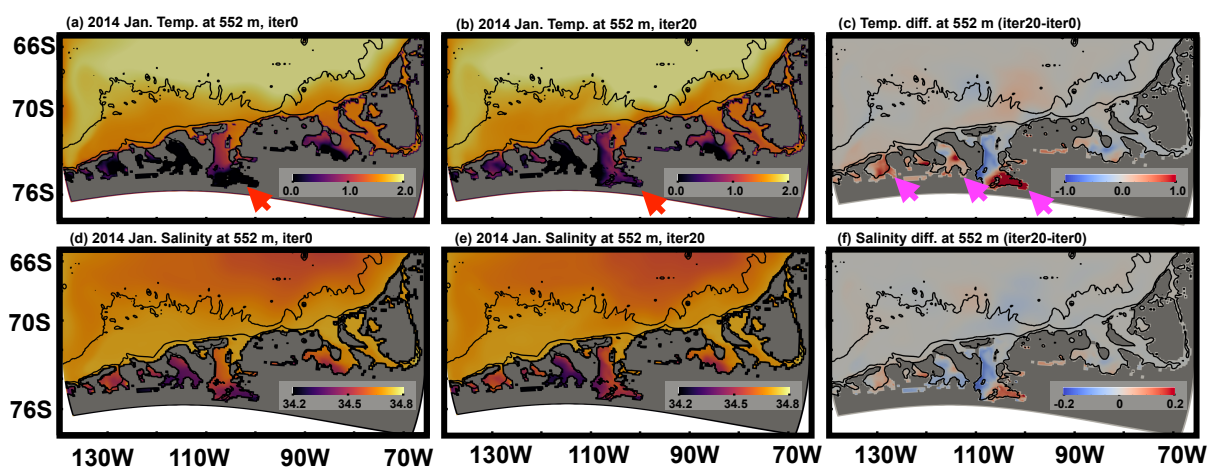


**Figure 6.** Simulated monthly mean (a,b) potential temperature and (d,e) salinity at 552 m depth in January 2014 for (left) unoptimized and (middle) iteration 20 simulations, respectively. (c) Potential temperature and (f) salinity differences between unoptimized and iteration 20 simulations. Bathymetric contours of 500, 2000, and 4000 m are shown in black. Red arrows indicate the PIIS front region and pink arrows indicate regions in the deep troughs in the AS. Potential temperature in these regions become warmer in iteration 20 simulation as mCDW intrusion into ice shelf cavities in the AS are correctly represented in the iteration 20 simulation.

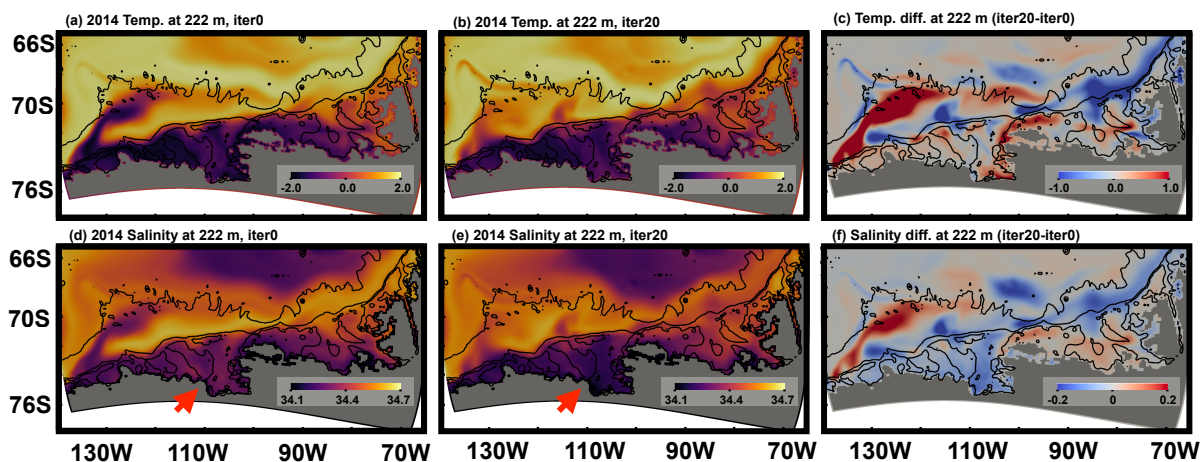


**Figure 7.** Simulated yearly mean (a,b) potential temperature and (d,e) salinity at 222 m depth in 2014 for (left) unoptimized and (middle) iteration 20 simulations, respectively. (c) Potential temperature and (f) salinity differences between unoptimized and iteration 20 simulations. Bathymetric contours of 500, 2000, and 4000 m are shown in black. Red arrows indicate the eastern AS region, where salinity becomes fresher by  $\sim 0.1$ , showing an improvement of WW properties.

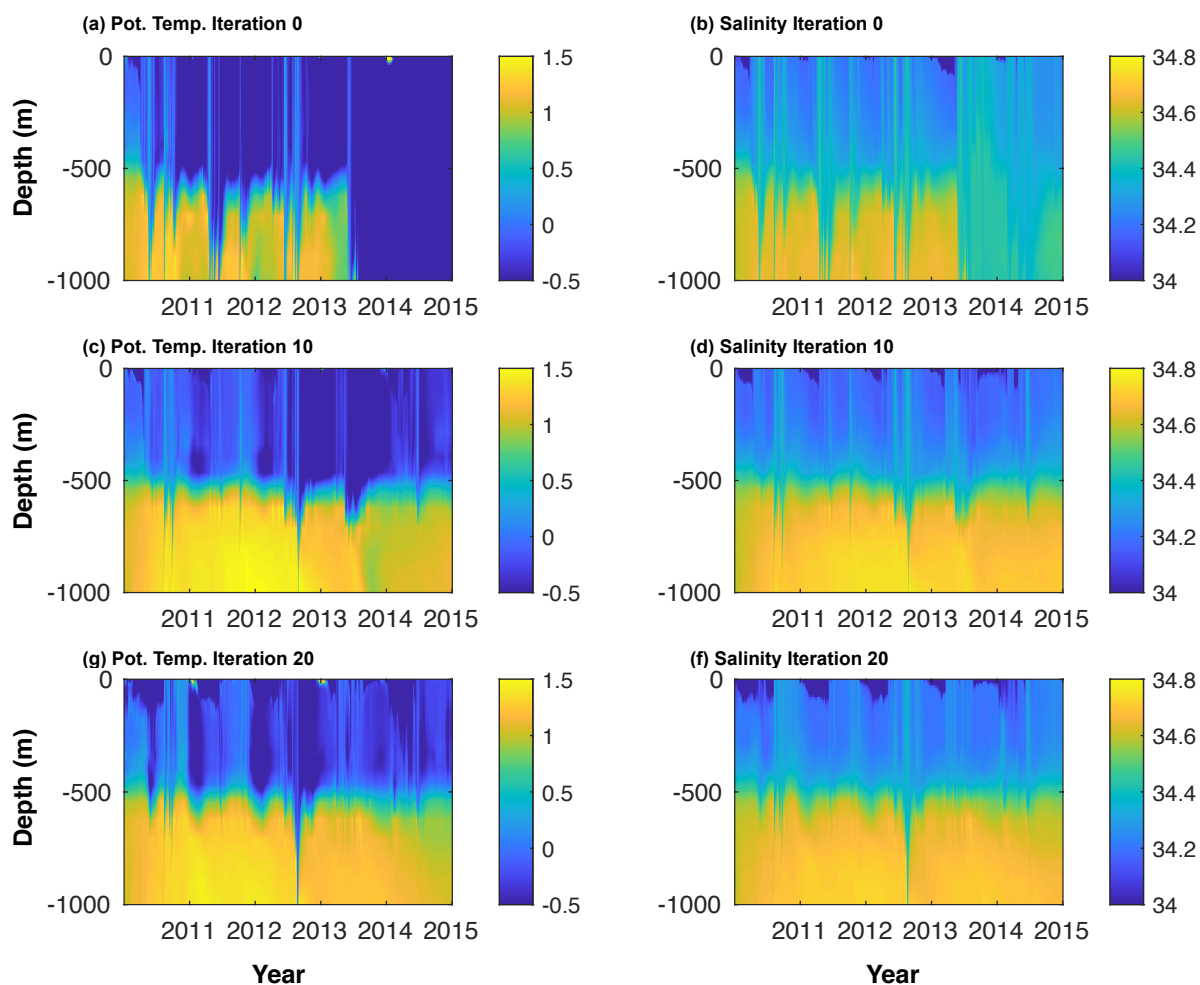


**Figure 8.** Simulated time series of (left) potential temperature and (right) salinity at BSR/iSTAR9 mooring locations for (a,b) iteration 0 (unoptimized), (c,d) iteration 10, and (g,f) iteration 20 simulations. Observed mooring timeseries are shown in Fig.12 and Fig.2c in Webber et al. (2017).

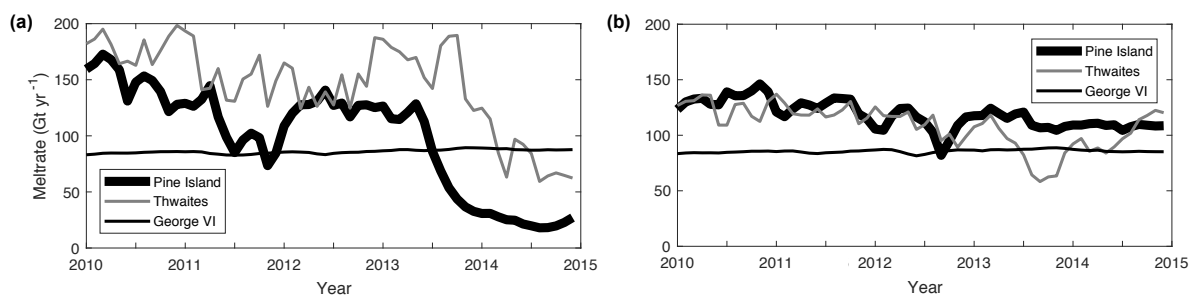


**Figure 9.** Simulated monthly mean basal melt rates from 2010 to 2015 for the Pine Island, Thwaites, and George VI Ice Shelves for (a) unoptimized and (b) iteration 20 simulations.

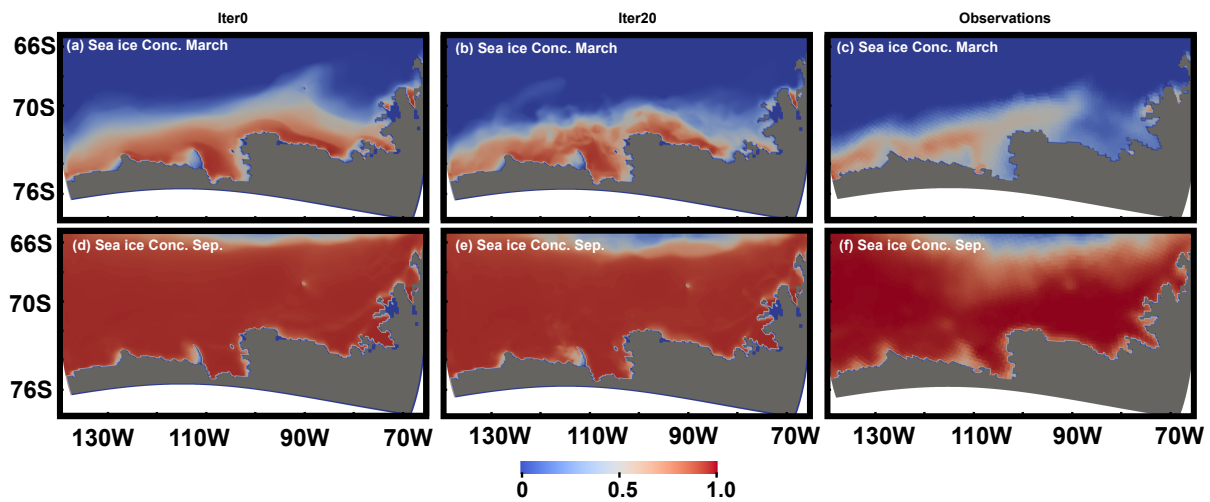


**Figure 10.** Simulated mean sea ice concentrations for (a,b) March and (d, e) September for unoptimized and iteration 20 simulations, respectively. The observed mean sea ice concentrations for (c) March and (f) September based on satellite sea ice concentration measurements between 2010–2014.

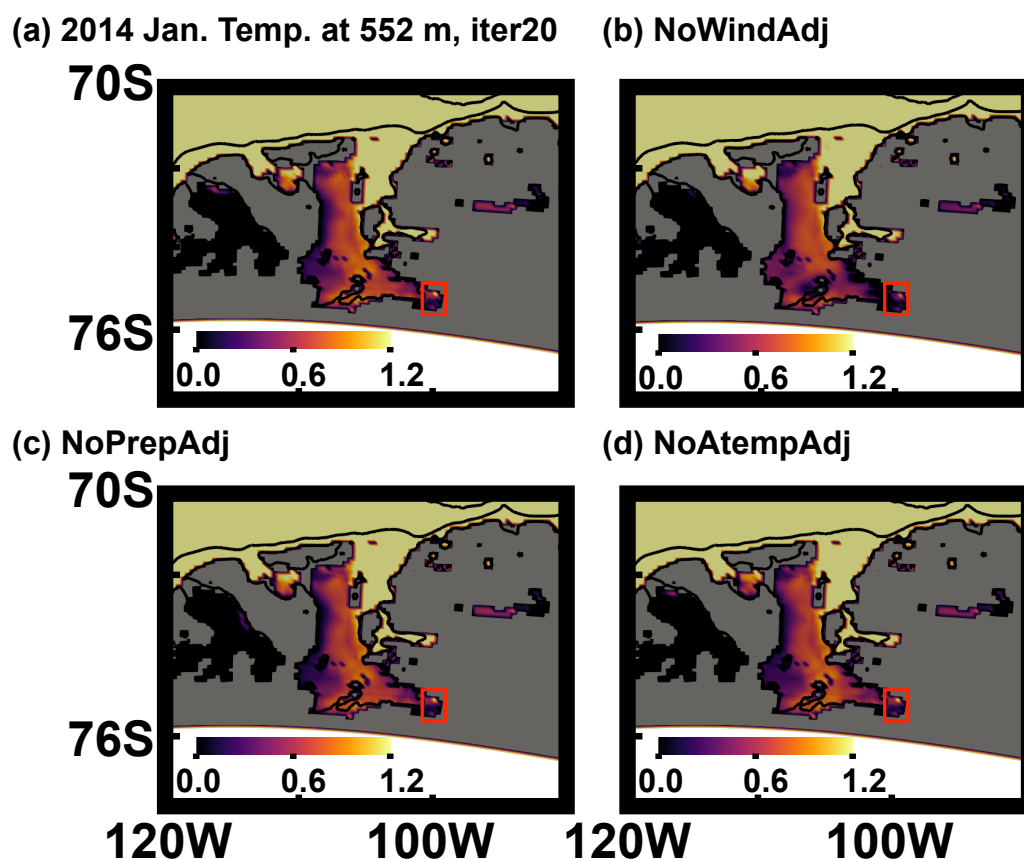


**Figure 11.** Simulated 2014 January mean 552 m potential temperature for (a) iteration 20, (b) NoWindAdj, (c) NoPrepAdj, and (d) NoAtempAdj simulations. Bathymetric contours of 500, 2000, and 4000 m are shown in black. Spatial averages of 552 m potential temperature are calculated for the region enclosed by the red boxes.



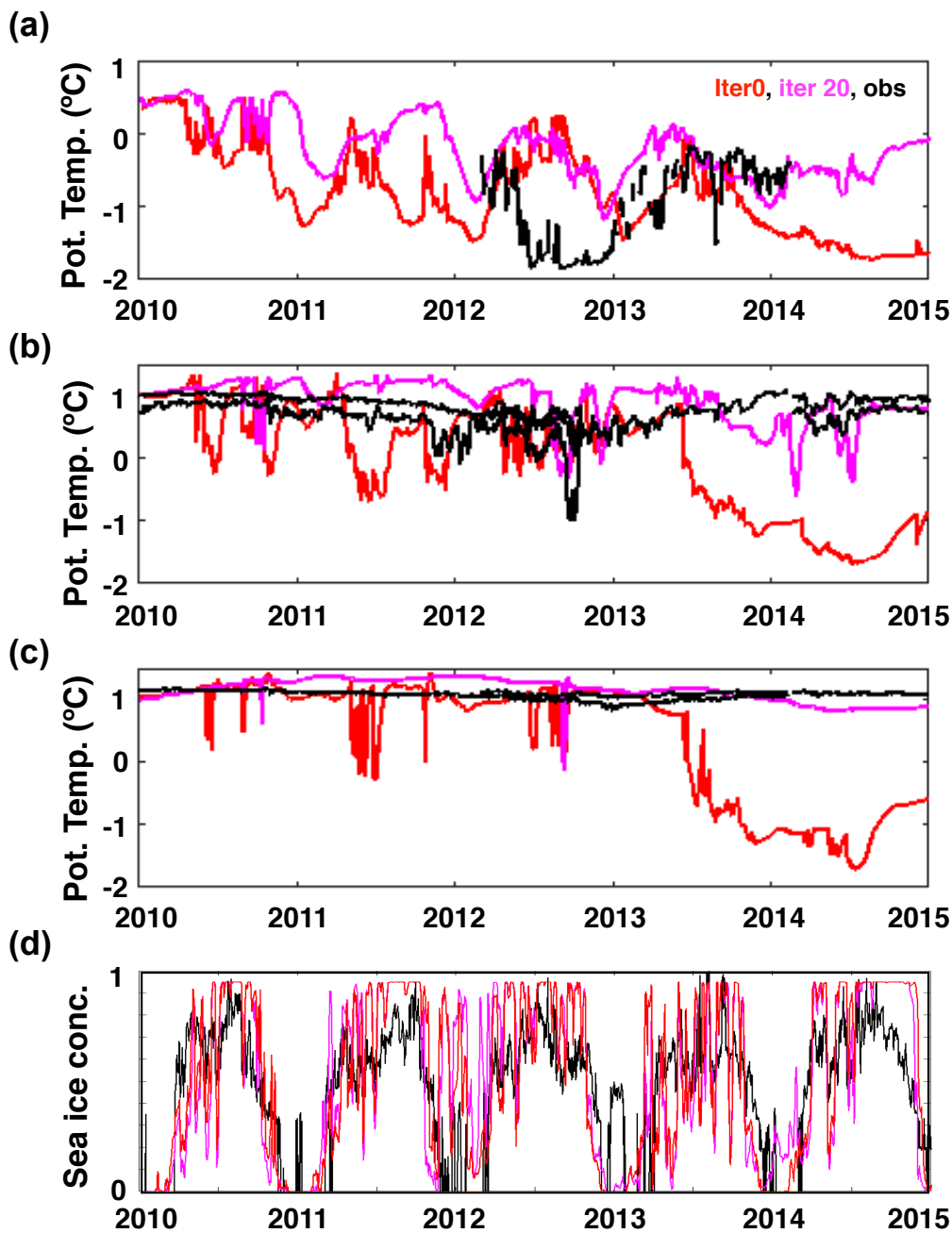


**Figure 12.** Time series of potential temperature at (a)477 m, (b)634 m, and (c) 909 m for unoptimized (iteration 0) and iteration 20 simulations. Time series of observed potential temperature at BSR5/iSTAR9 mooring sites at depths between (a) 400-500 m, (b) 600-700 m, and (c) 800-900 m are also shown in black. Time series of (d) spatially averaged (102.4-104.0°W, 74.8-75.0°S) sea ice concentration for unoptimized (iteration 0), iteration 20, and observations.



**Table 1.** Oceanographic datasets used for ocean state estimates.

Measurements	Year	Reference	Locations
Ship-CTD	2010	Nakayama et al. (2013)	AS
Ship-CTD	2010, 2011, 2012	Dutrieux et al. (2014); Kim et al. (2017)	AS
Ship-CTD	2014	Heywood et al. (2016)	AS
Ship-CTD	2010–2014	e.g., Ducklow et al. (2012)	BS
Mooring	2010–2014	Webber et al. (2017)	AS
Mooring	2012–2014	Kim et al. (2017)	AS
Seal-CTD	2014	Mallett et al. (2018)	AS
Sea ice concentration	2010–2014	Cavalieri et al. (1996)	AS, BS

**Table 2.** Model parameters used for ocean simulations. Most parameters are chosen based on Nakayama et al. (2017) and Zhang et al. (2018) with some adjustments.

Parameter	
Horizontal diffusivity ( $\text{m}^2 \text{s}^{-1}$ )	10
Background horizontal viscosity ( $\text{m}^2 \text{s}^{-1}$ )	1000, 500, 100, 10
Leith biharm non-dimensional viscosity factor	0.0
Modified Leith biharm non-dimensional viscosity factor	0.0
Background vertical diffusivity ( $\text{m}^2 \text{s}^{-1}$ )	$5.456 \times 10^{-6}$
Background vertical viscosity ( $\text{m}^2 \text{s}^{-1}$ )	$1.0 \times 10^{-4}$
KPP critical bulk Richardson Number	0.3273
KPP local Richardson Number limit for shear instability	0.8358
Bottom drag coefficient	$2.1 \times 10^{-3}$
Ocean/air drag coefficient scaling factor	0.508
Air/sea ice drag coefficient	$1.0 \times 10^{-3}$
Sea ice/ocean drag coefficient	$5.69 \times 10^{-3}$
Sea ice salt concentration	4.0
Stanton number (stable)	0.0492
Stanton number (unstable)	0.02506
Dalton number	0.0520
Lead closing (m)	1.24
Ice strength ( $\text{N m}^{-2}$ )	$1.0 \times 10^4$
Sea ice dry albedo	0.84
Sea ice wet albedo	0.78
Snow dry albedo	0.90
Snow wet albedo	0.80



**Table 3.** Adjustments to model parameters in addition to optimization using adjoint sensitivities.

Iterations	Adjustment
Iteration 10	change background horizontal viscosity from $1000 \text{ m}^2 \text{ s}^{-1}$ to $500 \text{ m}^2 \text{ s}^{-1}$
Iteration 11	heat and salt transfer coefficients for PIIS and Thwaites ice shelf reduced by 70% and 63%, respectively
Iteration 15	change background horizontal viscosity from $500 \text{ m}^2 \text{ s}^{-1}$ to $100 \text{ m}^2 \text{ s}^{-1}$
Iteration 20	change background horizontal viscosity from $100 \text{ m}^2 \text{ s}^{-1}$ to $20 \text{ m}^2 \text{ s}^{-1}$

**Table 4.** Satellite-based estimates of basal melt rate (Rignot et al., 2013) and model mean basal melt rates (2010–2014) for West Antarctic ice shelves for iteration 20. The values of heat transfer coefficient  $\gamma_T$  used for the optimized simulation are also shown.

Name	$\gamma_T$ (iterations 0–10) ( $\times 10^{-4} \text{ m s}^{-1}$ )	$\gamma_T$ (iterations 11–20) ( $\times 10^{-4} \text{ m s}^{-1}$ )	Observation based estimates (Rignot et al., 2013) ( $\text{Gt yr}^{-1}$ )	Optimized simulation ( $\text{Gt yr}^{-1}$ )
George VI (Geo)	0.11	0.11	<b><math>89.0 \pm 17</math></b>	<b>85.6</b>
Wilkins (Wi)	0.11	0.11	<b><math>18.4 \pm 17</math></b>	<b>11.5</b>
Bach (Ba)	0.57	0.57	<b><math>10.4 \pm 1</math></b>	<b>11.8</b>
Stange (St)	0.35	0.35	<b><math>28.0 \pm 6</math></b>	<b>33.0</b>
Ferrigno (Fe)	2.2	2.2	<b><math>5.1 \pm 2</math></b>	<b>1.7</b>
Venable (Ve)	0.35	0.35	<b><math>19.4 \pm 2</math></b>	<b>20.0</b>
Abbot (Ab)	0.27	0.27	<b><math>51.8 \pm 19</math></b>	<b>53.0</b>
Cosgrove (Co)	0.079	0.079	<b><math>8.5 \pm 2</math></b>	<b>9.8</b>
Pine Island (PI)	1.25	0.86	<b><math>101.2 \pm 8</math></b>	<b>118.3</b>
Thwaites (Th)	0.91	0.57	<b><math>97.5 \pm 7</math></b>	<b>108.8</b>
Crosson (Cr)	15.2	15.2	<b><math>38.5 \pm 4</math></b>	<b>44.0</b>
Dotson (Do)	3.3	3.3	<b><math>45.2 \pm 4</math></b>	<b>40.6</b>
Getz (Get)	0.26	0.26	<b><math>144.9 \pm 14</math></b>	<b>128.1</b>

**Table 5.** Description of all the sensitivity simulations.

Case	
NoWindAdj	iteration 20 simulation but excluding adjustment for wind
NoPrepAdj	iteration 20 simulation but excluding adjustment for precipitation
NoAtempAdj	iteration 20 simulation but excluding adjustment for air temperature